

# Multiscale modeling of transferrins and bovine serum albumin adsorption on coated gold and silver nanoparticles: the role of coating density and protein's glycosylation state.

*Julia Subbotina, Ian Rouse, Vladimir Lobaskin*

AUTHOR ADDRESS. School of Physics, University College Dublin, Belfield, Dublin 4, Ireland.

KEYWORDS. core-shell nanoparticles, gold nanoparticles, silver nanoparticles, PEGylated nanoparticles, bovine serum albumin, transferrin, protein adsorption, bio-nano interactions, multiscale modelling, molecular dynamics simulations, Monte-Carlo simulations, protein corona.

ABSTRACT. Polymer-coated nanoparticles are commonly used as drug carriers in nanomedicine. Their uptake rates are modulated by the interactions with essential serum proteins such as transferrin and albumin. Understanding the control parameters of these interactions is crucial for improving the efficiency of the nanocarriers. In this work, we perform a computational study of protein adsorption onto polymer (PEG) coated gold and silver nanoparticles. The applied approach yielded the protein-nanoparticle adsorption rankings onto coated as a function of PEG grafting density, which were validated against previously reported experimental protein-nanoparticle

binding constants. The *UnitedAtom* multiscale method also provides information on the preferred orientation of selected proteins immobilised on the surface of nanoparticles (nano-docking). The presented approach can be helpful for experimentalists working on the development of biosensors, nanocarriers, or other nanoplatforms where information on the preferred orientation of protein is crucial. It can also be used for fast pre-screening of various combinations of proteins, nanoparticles, and coatings (*in silico* bio nano assays).

TEXT. Zero-valent noble metal nanoparticles (NP) have attracted a lot of attention due to their unique physicochemical properties which make them suitable for use in theragnostic nanoplatforms<sup>1</sup>. Noble metal NPs are plasmon resonant and hold great promise as a contrasting reagent for tumour targeting and imaging<sup>2-4</sup> due to their strong and tuneable optical absorption. However, a vast number of metallic NPs are known to be toxic<sup>5</sup>. As a result, they are subject to a fast clearance from the bloodstream due to opsonization and recognition by the mononuclear phagocyte system (MPS) which suppresses the toxic impact by reducing the circulation time for the NPs. Such natural safety measures undermine the theragnostic potential of noble metal NPs as the response to the toxicity of the pristine core material prevents them from reaching a suitable level of theragnostic dose<sup>6</sup>.

Capping the metallic core with polymeric matter (e.g. with polyethylene glycol, PEG) was shown to improve the performance of metallic Au and Ag NPs for medical applications due to reduced toxicity<sup>7</sup>, making these NPs a good prototype for designing non-toxic drug nanocarriers. The presence of the polymeric outer shell creates a stealth effect and reduces the opsonisation of the PEGylated NPs. This, in turn, improves the saturation kinetics of the NP, helping to reach proper blood plasma concentration levels and prolonging their circulation time<sup>8,9</sup>. The PEGylation of NPs

has become a gold standard strategy for regulating nanotoxicity and improving biocompatibility of engineered nanomaterials (NM) used in medical applications<sup>10-12</sup>. The cloaking effect of the shell on the surface of NPs does not cancel out the adsorption of blood plasma proteins entirely<sup>13</sup>. Several such proteins were reported to bind onto polymer-modified surfaces, e.g., the binding of clusterin to ovalbumin nanocarriers (OVA-NCs)<sup>14</sup>. Harnessing this phenomenon offers a path towards novel efficient nanocarriers.

The precision of drug nanocarriers is based on the energetic balance between interactions occurring at two individual interfaces. The first occurs at the protein-protein interface and is defined by a selective complementarity between a receptor expressed on the surface of a cell and the active site of a specific coupled protein. The second takes place at the bio-nano interface and is determined by selective non-covalent binding of the coupled protein onto the nanocarrier, ideally such that the active site remains free for binding to cell receptors. While the complementarity between the cell-surface receptor and the coupled protein mostly develops naturally, the optimization of binding characteristics between NPs and coupled proteins can be artificially controlled. However, the design of novel nanocarriers requires finding a working triad of a suitable NP, cell receptor, and coupled protein which produces a protein bound to the NP in the necessary orientation to allow the protein to also bind to the receptor, and systematic experimental search for an optimal nanocarrier triad for a specific receptor might be a tedious task.

The selectivity for binding events occurring at two interfaces can be described in terms of binding free energy ( $\Delta G_{bind}^{p-p}$  and  $\Delta G_{bind}^{p-NP}$ ) and equilibrium association constants ( $K_{eq}^{p-p}$  and  $K_{eq}^{p-NP}$ ). In principle, these parameters can be predicted theoretically with a high accuracy either by molecular dynamics (MD) combined with enhanced sampling approaches or by molecular docking

techniques. While several successful examples have been reported for protein-protein and protein-small molecule interactions<sup>15,16</sup>, the capacity of conventional *in silico* tools for predicting  $\Delta G_{bind}^{p-NP}$  for a relevant number of promising protein-NP combinations is limited due to the immense dimensionality of the atomistic models, broad variations in conditions applied for *in vitro* preparation of nanocarrier (e.g. pH or ionic strength), the diverse structures of ENMs (different surface chemistry, nanocomposites, etc.)<sup>17-19</sup> or simply due to the lack of theoretical parameters describing the inorganic NPs in simulations. Therefore, one has to resort to approximations.

Recently, we have presented a multiscale *UnitedAtom (UA)* approach for predicting protein adsorption affinities for nanoscale materials. We have parameterised biomolecular interactions with a range of materials including titanium dioxide, quartz, carbon nanotubes, multiple metals and oxides, and surface-modified graphene<sup>20-22</sup>. The *UA* method employs a coarse-grained (CG) approach and uses pre-calculated interactions between molecular fragments of biopolymers (e.g. amino acids (AA) in peptides) and the target NP material. The total protein-NP interaction potential is obtained by summation of individual interaction potentials for AAs of a specific protein in a 3D arrangement with the NP employing an additive pairwise scheme and extracting orientation-specific binding free energies from these potentials. The *UA* multiscale method requires less computational effort for predicting protein binding affinities as compared to conventional simulation methods and finds good agreement for the prediction of binding patterns of individual proteins<sup>22</sup>, enabling the simulation of competitive adsorption of multiple proteins<sup>23</sup>. In this work, we extend the *UA* method to coated NPs to include the effects of surface chemistry on protein adsorption without explicit recalculation of the input NP-AA potentials for modified surfaces, avoiding the need to recalculate the interaction potentials for each substrate and surface

functionalisation via lengthy MD simulations combined with AWT-Metadynamics, as was required for modified graphene<sup>24,25</sup>.

The extension of the *UA* method targets the adsorption of proteins onto composite NPs consisting of a solid core and a soft polymeric shell. To cover various possible core-shell structures, we introduce a “LEGO”-like modular approach (Figure 1). Within this scheme, the interaction between AA side chains analogues (SCAs) and components of the NP (including surface chemistry elements) is modelled via sets of separate potentials for the interactions between each SCA and a component of the NP. To test and validate this novel methodology, we have performed *UA* multiscale modelling of BSA and TRF (glycosylated and non-glycosylated (ngTRF) variants) protein adsorption onto PEGylated (poly(ethylene)glycol-coated) silver and gold core-shell NPs. These systems were previously reported by R. Barbir *et. al* and the protein binding characteristics for selected proteins were measured experimentally<sup>26</sup>.

## **Results and Discussion.**

The theoretical background for the *UA* model for core-shell NPs applied in this work is outlined in “Methods” section. Additional details on the construction methodology for the simulated protein-NP models (including PDB structures) used here can be found in *Supplementary materials*.

Since the exact adsorption free energy  $\Delta G_{bind}^{p-NP}$  values cannot be calculated within the *UA* framework<sup>22</sup> due to strong approximations, we have focused our study on the following model performance aspects: prediction of the stealth effect caused by PEGylation, accurate prediction of binding affinity ranking for PEGylated nanoparticles in relation to fragment resolution level of nanoparticle constructs, and reproduction of differences in protein adsorption of transferrin variants in individual adsorption experiments.

According to the reported CD spectra for the selected proteins<sup>26</sup>, their adsorption onto NPs did not result in drastic alterations of the globular protein structure, with only small to moderate changes in  $\alpha$ -helix,  $\beta$ -sheets, and the rest of the structure noted. This observation suggests that the *UA* model with a “rigid body” protein representation<sup>20-22</sup> should be suitable for predicting binding affinities for this case.

### **Predicting adsorption affinity rankings and stealth effect: the role of PEG grafting density.**

The experimental data suggest that the binding of transferrin variants to citrated gold and silver NPs with various diameters (13-60 nm) is weaker than the binding of bovine serum albumin to these NPs, with the exception of ngTRF adsorbed to smaller AuNPs<sup>26</sup>. However, the introduction of 5K PEG shell on the spherical AuNPs and AgNPs reversed the adsorption affinity rankings, making the naturally occurring glycosylated variant of transferrin the most strongly binding protein and the bovine serum albumin the weakest one. To explain the difference in binding affinities for coated and uncoated nanoparticles we have constructed multicomponent *UA* models of pristine and core-shell nanoparticles.

It is known that variations in the grafting density of polymeric coatings on the surface of a NP can influence protein adsorption considerably<sup>27</sup>. Elevated grafting density and/or high molecular weight of the polymer (high-density brush regime) was shown to enhance the antifouling characteristics of NPs by reducing protein adsorption<sup>28-30</sup>. Since no information was reported on the morphology of the polymer layer, Flory’s theory<sup>31-33</sup> was employed to produce CG models of core-shell PEGAuNPs and PEGAgNPs (see the corresponding section in *Methods*). The theory suggests that the grafted polymer chains change their shape between two limiting-case conformations: the “mushroom” (low density) and the “brush” (high density) upon increase of the

grafting density  $\sigma$ . The mixed state of the polymer chain corresponds to the “intermediate” grafting density region. The boundary between “mushroom” and “brush” regimes is controlled by the ratio between the mean chain-to-chain distance on the NP surface  $D$  and Flory radius  $R_F$  for a single polymer chain. Four core-shell Ag and Au NPs with varying grafting densities of 5K PEG ( $\sigma = 0.01 - 0.65$  chains/nm<sup>2</sup>) were utilized for  $UA$  calculations of protein binding energies are shown in Figure 2. Two additional solid uniform NPs for each core material representing bare 35.7 nm Au and 52.7 nm Ag NPs (Figure 2, far left) and two solid PEG NP with equal diameters (Figure 2, far right) were added to the set for comparison purposes.

Protein adsorption rankings calculated with the  $UA$  model and experimentally observed ones are shown in Figure 3. The uncoated 52.7 nm Ag NPs exhibited stronger attraction of proteins as compared to 35.7 nm AuNPs. The gradual PEGylation of NPs from “pristine” to “brush” models resulted in weakening of protein adsorption and changing the binding pattern – the binding to smaller PEGAuNPs was stronger than for larger PEGAgNPs. The predicted overall decrease of protein adsorption affinities due to coating of pristine NPs is a result of the stealth effect commonly observed for PEGylated NPs<sup>14,34–36</sup>, which arises from the weaker binding of proteins by PEG itself and shielding of the metallic core by the PEG chains. The calculated protein adsorption affinities as a function of PEG grafting density was found to be non-monotonic (Figure 4), similar to the pattern previously reported by Walkey et al.<sup>35</sup>. Those authors have also found that at the lower PEG grafting density the adsorption of high-molecular-weight serum proteins was suppressed, while at higher grafting density their adsorption prevailed while for smaller NPs with fixed PEG grafting density the overall adsorption of proteins increased<sup>35</sup>. In our calculations, the increase in grafting density (and decrease of metallic core radii) resulted in improved binding of larger (ca. 80 kDa) transferrins to smaller 35.7 nm PEGAuNPs in high density “brush” model,

while the interaction between lighter (ca. 66 kDa) BSA protein and larger 52.7 nm PEGAgNPs was the weakest. The calculated magnitude of the PEG shielding effect for BSA was approx.  $40 - 60k_B T$  and approx.  $40 - 50k_B T$  for transferrins (“pristine” vs. “brush” models). Similar conclusions on protein adsorption trends associated with the increase of PEG brush density can be also drawn from the orientation-specific adsorption energies for PEGAuNPs and PEGAgNPs shown as heatmaps in Figures 5 and 6. Thus, the interplay between the factors mentioned above (protein molecular weight, PEG grafting density, and nanoparticle radii) ultimately results in changes in the protein adsorption affinities, which in the case of PEGylated gold nanoparticles were found to be more significant for transferrins than for BSA. Adsorption of TRF on PEGAuNPs was ca.  $10k_B T$  stronger as compared to PEGAgNPs.

Overall, we get the best match between the experiment and the simulation in terms of relative and absolute affinities using the raspberry model at the “intermediate” grafting density (Figure 3), which apparently most accurately reflects the properties of the PEG coating in the experiment, thus providing the otherwise unknown molecular details. A one-bead-one-material “shell\_solid” model of the PEG outer layer, equivalent to the original single-component *UA* model,<sup>20–22</sup> was also able to reproduce protein adsorption affinity ranking that matched experimental data (Figure 3). However, the calculated absolute values of binding energies were substantially underestimated: the adsorption of BSA was predicted to be slightly endothermic ( $E_{ads} \approx 0.3k_B T$ ) and a small exothermic effect was predicted for adsorption of transferrins ( $E_{ads} \approx -1k_B T$ ). We attribute this to a limitation of the solid NP model which does not allow for a sufficient number of interfacial contacts between PEG and the rigid protein, which are obviously present for the “intermediate” grafting density model. Using a more detailed representation of the PEG-only NP did not lead to significant improvement of the binding energy compared to experimental values, however

the “shell\_solid\_raspberry” model (Figure 1, model *d*), composed of a single solid PEG central bead and a thin layer of PEG raspberry beads, produced slightly better estimates of exothermic binding affinities matching the experimental ranking of proteins adsorption affinities.

As can be seen in the adsorption heatmaps (Figures 5 and 6) the preferred orientations of bound proteins on the NPs are similar across both materials and the same compositional combinations of a metallic core and PEG shell. Examples of docked structures for protein adsorption complexes corresponding to the most strongly adsorbing configurations for “custom” grafting density model are shown in Figure 7.

The assumptions on polymer grafting densities used in our calculations were made based on limited experimental input and thus are subject to some arbitrariness. Thus, their simplicity might partially impact the overall conclusions. From this perspective, we would like to stress the importance of full reporting of physicochemical parameters/conditions used in the experiments with NPs<sup>37</sup>, as these data could provide a better background for consistent theoretical models.

### **Impact of glycosylation state of transferrin on adsorption affinities.**

The predictions of the *UA* model were also sensitive to the presence of posttranslational modifications in the protein, e.g. glycosides in TRF vs. the absence of those in ngTRF. This sensitivity was dependent on the modelling resolution of PEG brush density. In the case of the high-density brush model, the interaction of non-glycosylated ngTRF was predicted stronger than one for the glycosylated variant. The decrease of PEG grafting density (“custom” and “intermediate” grafting density models in Figure 3) led to a higher exothermic effect of adsorption for TRF as compared to ngTRF (ca.  $2.5k_B T$  in the intermediate grafting density model).

The favored binding of glycosylated TRF arising from surface polymer shell modification of metallic NPs can be linked to the synergy between the hydrophilic nature of PEG and carbohydrate fragments. Although it is reasonable to expect that glycans might improve the TRF adsorption because of direct interaction with the PEG outer layer, the arrangement of adsorption complexes of transferrin variants immobilized on modelled NPs reconstructed from the *UA* output did not fully support it (Figure 8). Two common lowest energy conformations were identified corresponding to transferrins' preferred orientations on pristine or coated gold or silver nanoparticles. They were identified at ( $\phi = 10^\circ$ ;  $\theta = 155^\circ$ ) and ( $\phi = 230 - 235^\circ$ ;  $\theta = 30 - 35^\circ$ ) rotational angles. For these orientations, only two to three *N*-linked glycan fragments were close to the PEG surface of the nanoparticle (Figure 8, glycan fragments highlighted in green), while the remaining five to six glycans were directed outwards. The increase of polymer grafting density did not qualitatively alter the protein adsorption fingerprints for either core material (Figures 5 and 6), except for the adsorption energy minimum at ( $\phi = 10^\circ$ ;  $\theta = 155^\circ$ ) rotational coordinates, which became more pronounced at higher  $n_{CG}$  values as compared to other alternative orientations. It should be also noted that in some cases multiple orientations can correspond to similar structures, e.g., the two local minima for TRF at ( $\phi = 10^\circ$ ;  $\theta = 155^\circ$ ) and ( $\phi = 40^\circ$ ;  $\theta = 135^\circ$ ). The obtained preferred orientations of bound TRF suggest that the glycans present in this protein, which in general are known to reside mostly on the exterior of proteins, are expected to remain accessible for further interactions after adsorption onto a NP. A similar behavior was observed experimentally for the formation of protein corona on citrate-stabilized gold NPs where glycosylated fragments on adsorbed proteins remained accessible for further modifications<sup>38</sup>.

The overall elevated binding affinity of glycosylated TRF at low grafting densities can be explained by an additional effect associated with stronger binding calculated for Ag and Au slabs

and individual glycan fragments (see previously reported  $A_g$  values in work <sup>39</sup> and Figures S4 and S5 for  $A_u$  values in *Supplementary Materials*). For example, for Au FCC (111) the adsorption energies for carbohydrates were ca.  $-20 - 25k_B T$  while for AA SCA the adsorption energies were in the range  $-1 - 28k_B T$ . At the same time, the interaction with PEG was even weaker than the NP-AA interaction (at ca.  $0.4 k_B T$ , Figure S7 in *Supplementary Materials*). However, as the energy estimate by the *UA* method includes contributions from all rotational/translational configurations (including statistically less relevant penalized orientations with close contacts between glycans and metallic/PEG CG beads), these extra contributions result in an increased  $E_{ads}$  term for glycosylated proteins. Furthermore, the thinner the PEG layer and the more accessible the metallic core to the glycans, the stronger this added stabilization will be. From this it can be also concluded that proteins with a greater fraction of glycosylated residues accessible for the interactions with the NP are expected to have a stronger binding to the  $A_g$  or Au surface.

In the case of TRF, which contains only a small number (8) of N-glycan fragments, glycosylation-assisted binding is not expected to be crucial for protein adsorption onto coated NPs with 3-8 nm thick PEG layer. Instead, it is more likely that cooperative interaction of AA sidechains with the NP will control the total protein adsorption affinity. The reported experimental data<sup>26</sup> on binding constants for transferrins immobilized at other functionalized AuNPs/AgNPs partially (subject to differences in size, shape, surface charges, etc. for studied nanoparticles) supports this prediction: non-glycosylated ngTRF was shown to have a stronger interaction as compared to its glycosylated version in general.

In summary, we find that PEG coating changes the protein adsorption on NPs in several aspects. Most of all, it reduces the binding strength thus providing the stealth effect, in agreement with experimental observations. Secondly, it changes the binding affinity ranking, so we register

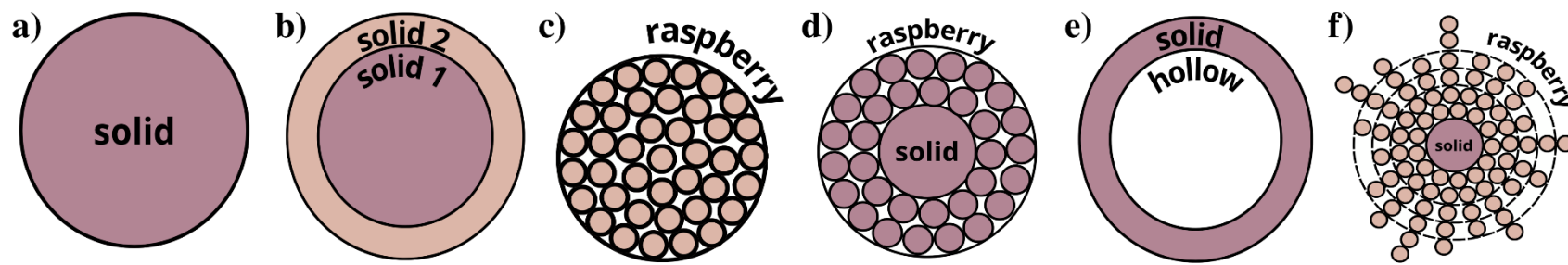
different binding preferences at different PEG grafting densities. This alteration should affect the content of the NP protein corona. We see evidence that the corona is determined by multiple factors such as the grafting density and molecular weight of the grafted polymers, protein type, and its glycosylation state. Also in agreement with experimental data, we show that glycosylation of a protein enhances the overall interaction with PEGylated and pristine noble metal NPs. The overall trend is a result of an interplay of various factors (accessibility of N-glycans for interaction with a metallic surface, configurations of the PEG chains, the AA composition of the protein, etc.). This observation suggests that glycans, and possibly other protein modifiers (e.g., lipid fragments in lipoproteins), should be taken into account for modeling bio-nano interfaces existing in physiological conditions. Potentially, glycosylation-assisted protein adsorption may be used as a strategy to develop sensitive analytical nanoplatfroms for detecting blood protein markers in diabetic patients<sup>42</sup> or viruses containing glycan-rich patches on their exterior<sup>43</sup>. The predicted stronger overall adsorption of glycosylated proteins onto uncoated and coated NPs also leads to questions about how metabolic syndromes<sup>44</sup> can impact the efficiency nanomedicine in patients as a result of altered bioaccumulation of NPs and associated adverse outcomes linked to such changes.

## **Conclusions.**

We performed a multiscale computational study of protein binding on to PEG-functionalized gold and silver NPs. For this purpose, we have introduced a new modular CG model of a coated NP, which is capable of representing a variety of typical core-shell nanostructures used for drug delivery. The predictions of protein affinity ranking are in line with available experimental data. Moreover, based on comparisons with experimental data, we were able to obtain molecular lever

insights into the structure of the polymer coat and preferred protein orientation that are not accessible experimentally. As the calculations with this multiscale approach are very fast once the materials and interactions are parameterized, this method can be used for high throughput *in silico* screening of protein adsorption onto core-shell NPs for the rational design of drug nanocarriers and nanobiosensors<sup>40,41</sup>. While qualitative predictions of protein adsorption can be obtained already with a uniform density representation of the NP, a more detailed representation of core-shell noble metal NPs including the molecular structure of the coating is necessary for more accurate investigations into protein corona content and bound protein activities. The raspberry model of the NPs can be applied to study nanocarriers of high structural complexity. The structures of protein-NP complexes obtained using our model can be used as initial estimate coordinates for further computational refinement, aiding in the precise design of drug nanocarriers and nanobiosensors where the information on the orientation of the immobilized protein is important.

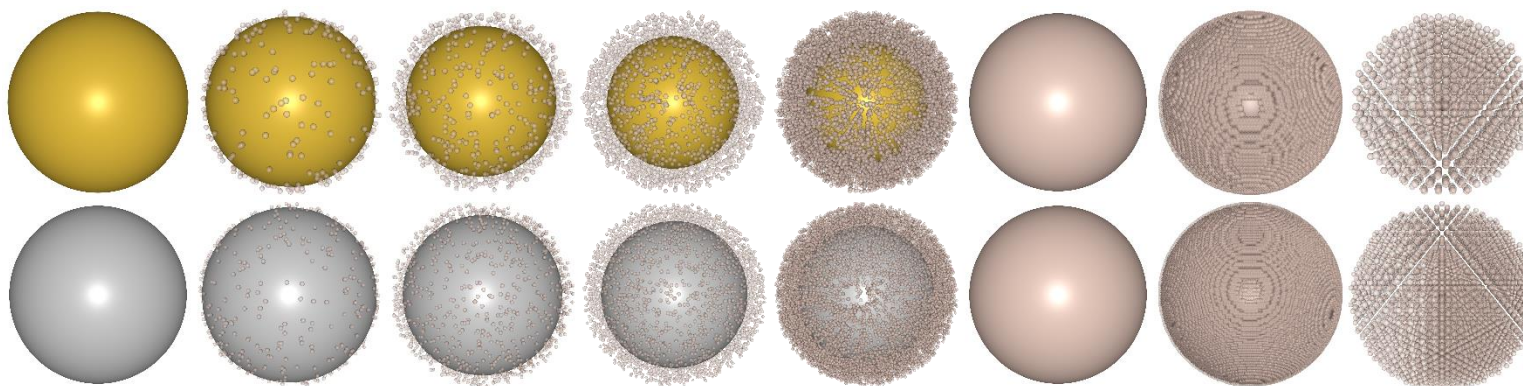
**Figure 1.** “LEGO” models of multicomponent NPs which can be simulated in the extended version of the *UnitedAtom*



- a. Uniform density solid single material NP (original version<sup>21,45</sup>)
- b. Composite NP made of  $n$ -layers of solid materials with uniform density (extended version)
- c. Raspberry model single material NP (extended version).
- d. Raspberry outer layer - solid core single material NP (extended version)
- e. Solid uniform density outer layer - hollow core single material NP (extended version)
- f. Raspberry outer layer - solid core dual material NP (extended version)

Raspberry models (*c, d, f*) may be used for representing nanocomposites, heteropolymers or mixed coatings. In this case different potentials corresponding to different components of the NP should be assigned to the raspberry beads.

**Figure 2.** CG structures of pristine and PEGylated Au and Ag NPs utilized for  $UA$  calculations.

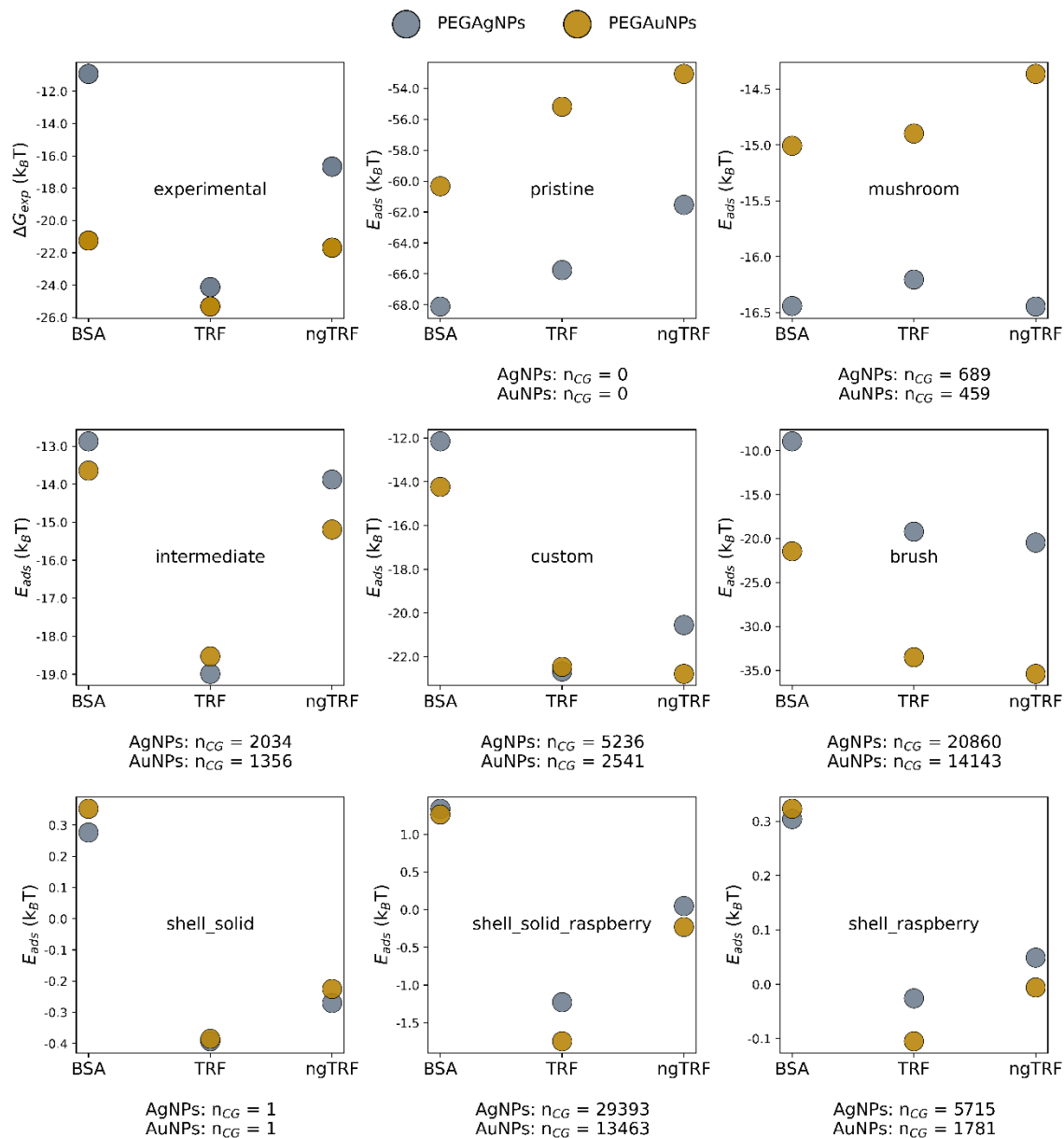


Top row – CG models of gold NPs, bottom row - CG models of silver NPs

Naming convention of CG models, from left to right:

- “*pristine*”
- “*mushroom*”
- “*intermediate*”
- “*custom*”
- “*brush*”
- “*shell\_solid*”
- “*shell\_solid\_raspberry*”
- “*shell\_raspberry*”

**Figure 3.** Adsorption energies for pristine and PEGylated Au and Ag NPs.



\*The experimental value of the adsorption free energy ( $\Delta G_{exp}$ ) was evaluated via  $\Delta G = -RT \ln K_B$

**Figure 4.** Non-monotonous variation of protein adsorption affinities as a function of the coating density.

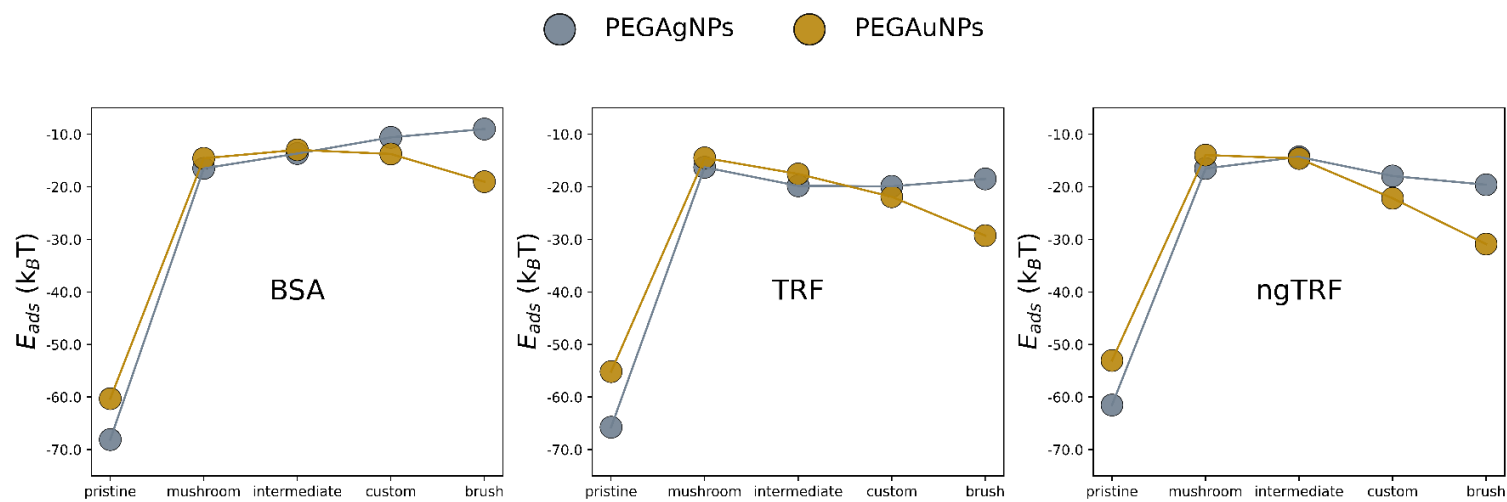


**Figure 5.** Adsorption heat maps for TRF, ngTRF, and BSA proteins adsorption onto pristine and PEGylated AuNPs.

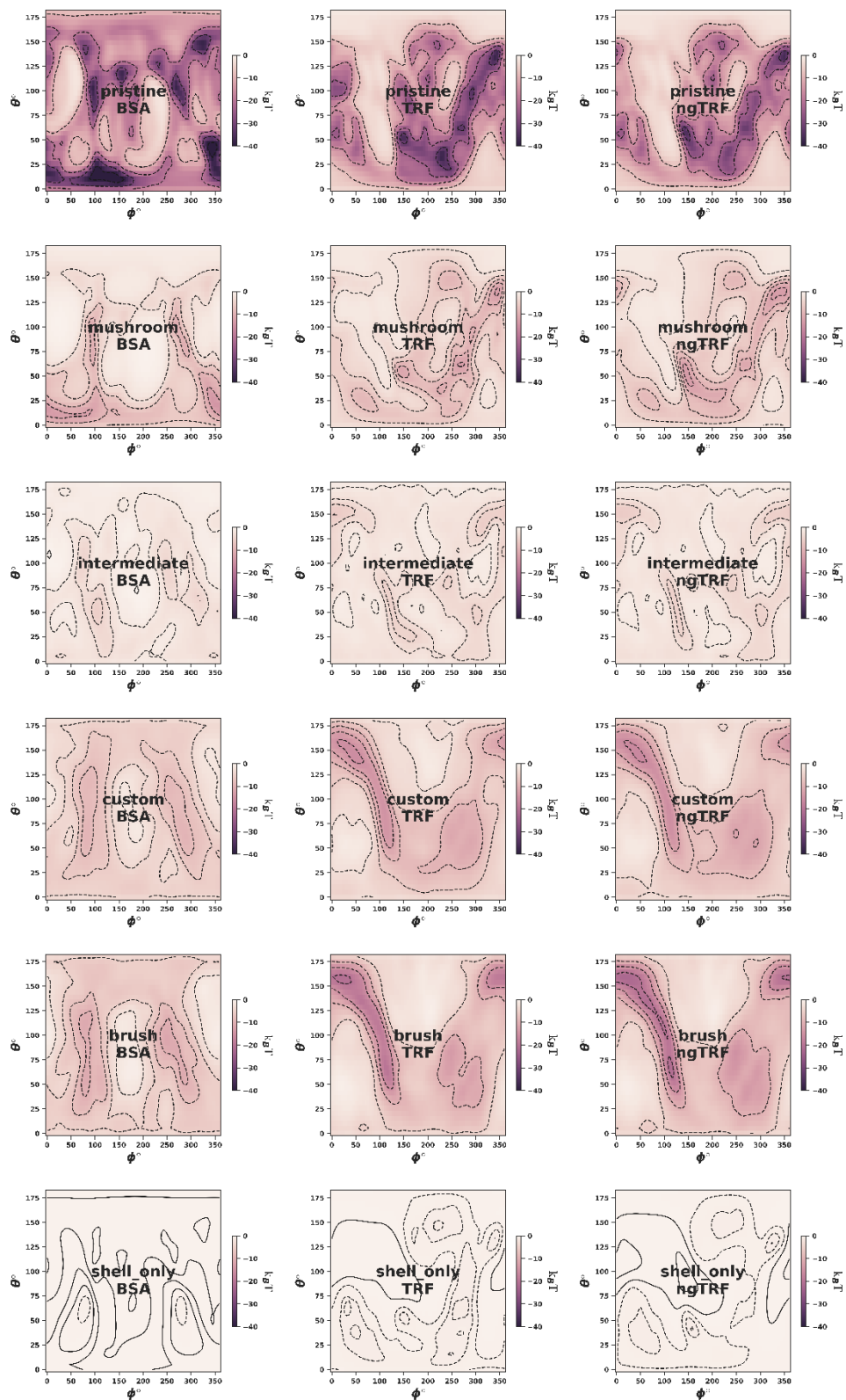


**Figure 6.** Adsorption heatmaps for TRF, ngTRF, and BSA proteins on pristine and PEGylated AgNPs.

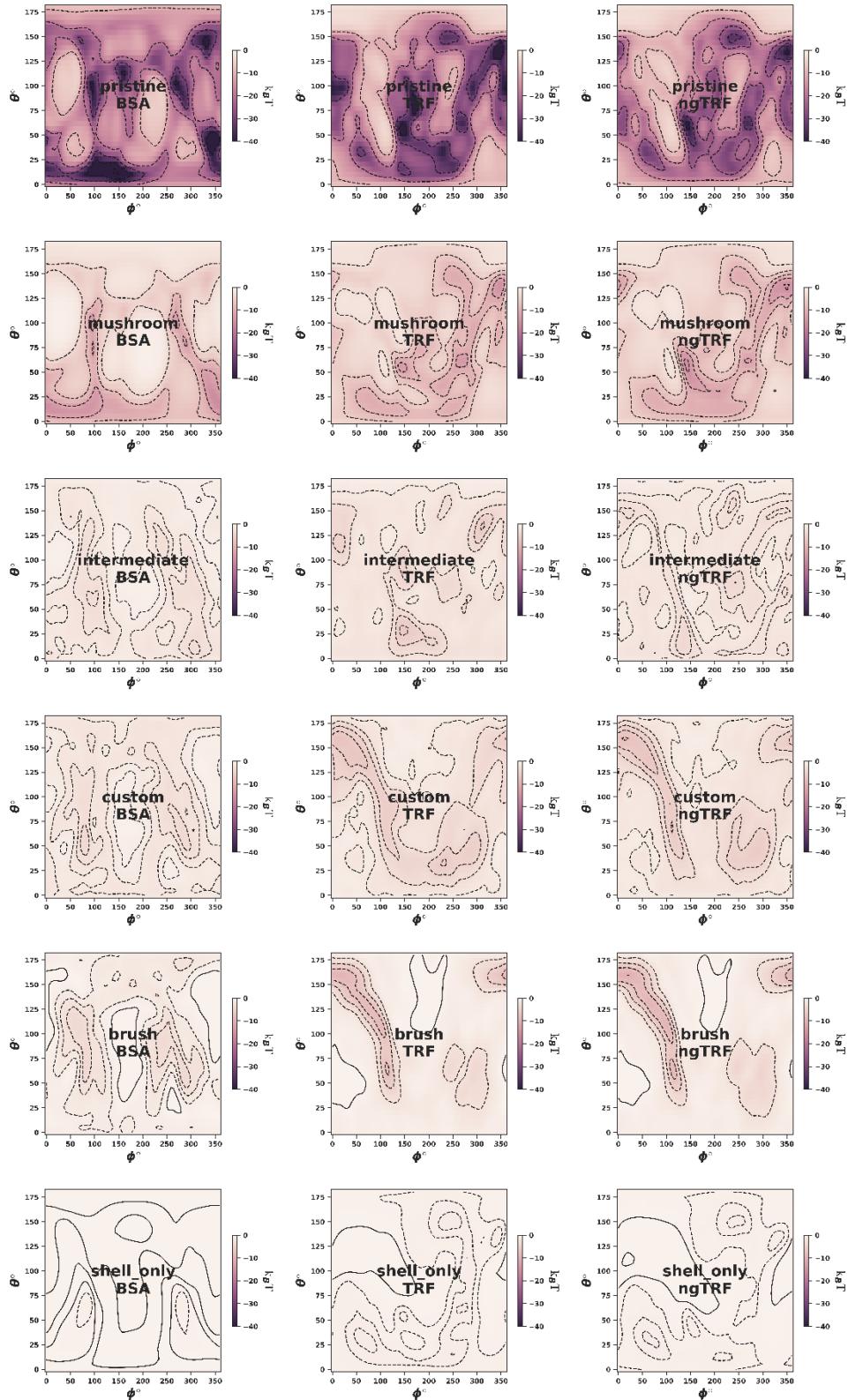


**Figure 7.** Lowest energy configurations of adsorption complexes for TRF, ngTRF, and BSA proteins onto PEGAuNPs and PEGAgNPs with dense PEG brush density (“custom” model).

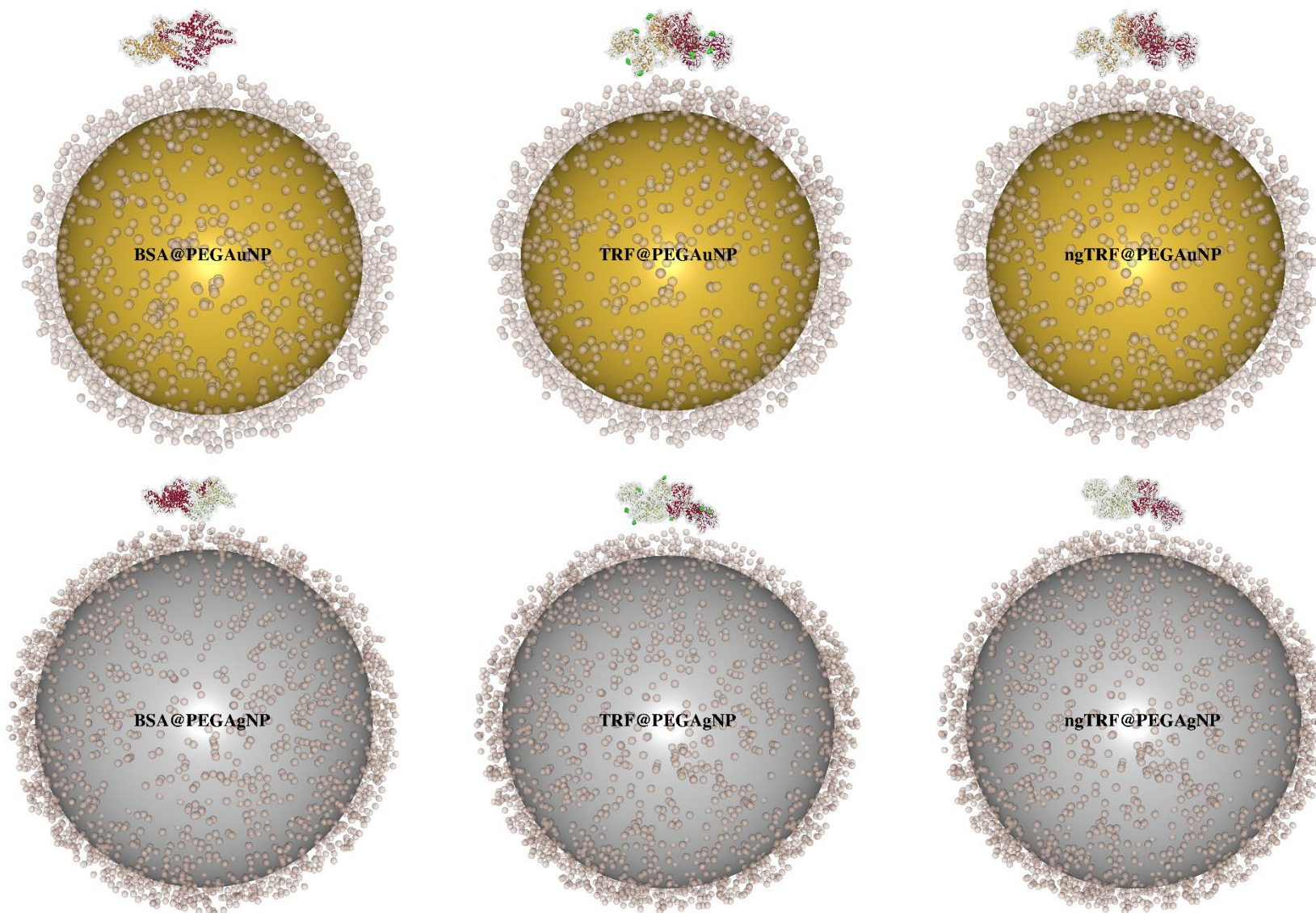
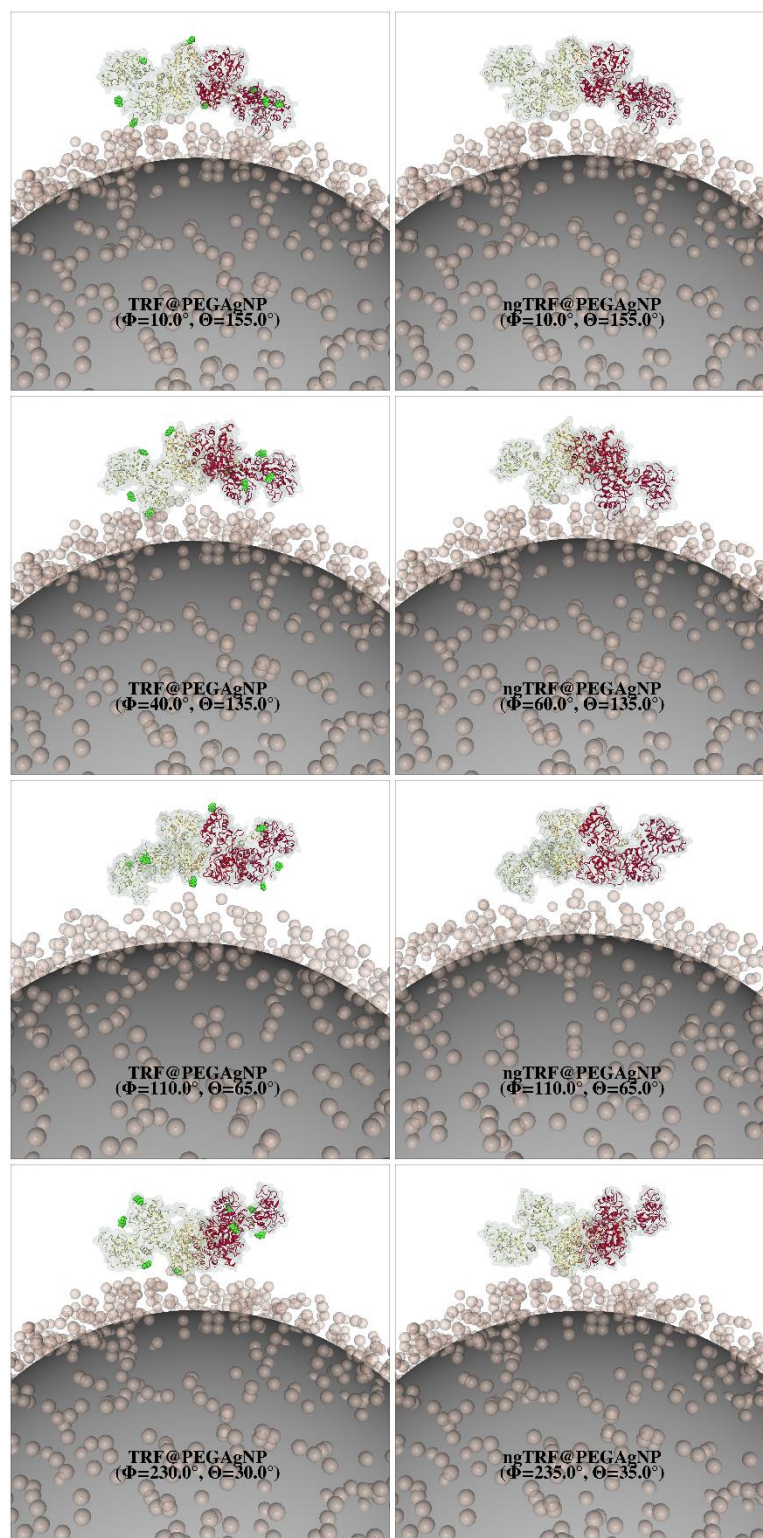


**Figure 8.** Configurations of adsorption complexes of TRF/ngTRF at PEGAgNPs with “intermediate” PEG brush density corresponding to the identified minima of adsorption energy landscape.



## Methods.

### Overview of the *UnitedAtom* multiscale method.

Here, we briefly describe the *UnitedAtom* model for the prediction of protein-NP binding energies. The original method considers variously shaped NPs as homogeneous entities with uniformly distributed density across the NP volume. The interaction between an NP and a rigid protein is presented as a sum of electrostatic and short-range nonbonded (including e.g, van der Waals, dipolar, and excluded volume effects obtained from atomistic MD simulations) interactions, the energy of which is calculated through a summation of corresponding interaction energy terms between each AA and the NP:

$$U_{P-NP} = \sum_{i=1}^{N_{AA}} U_i^{AA-NP}(d_i(\theta, \phi)) = \sum_{i=1}^{N_{AA}} (U_i^{el}(d_i(\theta, \phi)) + U_i^{nb}(d_i(\theta, \phi)))$$

It should be pointed out that interaction between the NP and the protein backbone in the *UA* model is not included in the short-range interaction potential and only factors into the long-range van der Waals potential. More details on the theoretical background for the *UA* model can be found in the original publications<sup>20-22</sup>.

In the present work, we extend the model to composite NPs with non-uniform density, e.g. multi-component NPs with various polymeric coatings or core-shell NPs. This is achieved by representing a complex NP as a set of smaller building blocks (“NP components”), parameterization of their interactions with AAs, and summing the above potentials over all the NP components, similar to the summation of the NP-AA potential over all the AA beads in a protein. Each NP component is described using the same set of parameters employed for the initial *UnitedAtom* model together with a set of coordinates describing the center of each component and

an overall scaling factor for the potentials contributed by this component. Complex NP structures are assembled from combinations of these components, with negative scaling factors used to allow for the representation of hollow NPs or shells by subtracting a smaller NP from a larger one. Surface-modified NPs are represented as a set of beads of the brush material surrounding the core bead(s). Combinations of these shapes enable the simulation of complex NPs as shown in Figure 1. If required, large NPs can be represented by a raspberry-like construction to produce a more realistic model at the cost of an increase in computational time. This methodology assumes that the NP-AA potential is isotropic over the surface of the NP, which is not the case for low-density brushes in which all AA beads of a given type have the same potential despite potentially having very different environments, e.g. direct exposure to the core or exposure to a brush only depending on their location in the protein. To mitigate this effect, we apply an additional hard-shell potential between brush beads and AA beads to penalise configurations with unrealistic protein-brush overlaps and average over NP orientations as discussed later.

### **Generation of coarse-grained coordinates for core-shell nanoparticles.**

In the present study, the polymeric shell is represented by a set of CG beads with a size equal to twice the radius of gyration of polymer fragments used in the *UA* model (see the corresponding section below). In the current case, we used PEG trimers to represent a full-length chain of PEG 5K. CG models of PEG layers were constructed through a stochastic algorithm by placing PEG beads to match the target density profiles reflecting differences in grafting densities (Figure 1, model *f*). This method allows the modeling of polymeric core-shell NPs with various grafting densities of the polymeric outer layer.

We chose the specific relationships between grafting density distance  $D$ , Flory radii  $R_F$  for individual polymer chains and the shell morphology (layer thickness and grafting density) as follows<sup>12</sup>:

$$\frac{R_F}{D} = \begin{cases} 4.0, & \text{high – density coating,} & \text{"brush" regime} \\ 2.0, & \text{medium – density coating,} & \text{"intermediate" regime} \\ 0.5, & \text{low – density coating,} & \text{"mushroom" regime} \end{cases}$$

The experimentally measured Flory radius for PEG5K was  $R_F = 5.6$  nm. From this, the area of the surface occupied by one chain is equal:

$$A = \frac{\pi D^2}{4},$$

and the grafting density (number of chains per nm<sup>2</sup>) then:

$$\sigma = \frac{1}{A} = \frac{4}{\pi D^2}.$$

The thickness of polymer layer can be estimated as:

$$L = N \left( \alpha^{5/3} \right) \sigma^{2/3},$$

where  $\alpha$  is the length of the monomer ( $\alpha = 0.35$  nm for PEG unit<sup>8</sup>) and  $N$  is the number of monomer units ( $N = 113$  for PEG5K). This gives grafting densities and the thickness of PEG layer as presented in Table 1.

**Table 1.** Predicted grafting density ( $\sigma$ ) and corresponding thickness of polymer layer ( $L$ ).

regime	“mushroom”,	“intermediate”	“brush”
$\sigma$ (chains/nm <sup>2</sup> )	0.01	0.16	0.65
$L$ (nm)	0.921	5.847	14.733

Considering that the density of the polymeric shell is not uniform, the placement of the PEG CG beads should be done according to the normalized density profile defined within the interval  $[0; L]$ . Experimental density can be used, as well as any other density profile defined analytically. For the current case the following arbitrary function ( $a = 4.0$  and  $b = 11.0$ ) was selected to reconstruct normalized density profile:

$$\rho(L) = \frac{1}{a + e^{b(L-0.5L)}}$$

$$\rho_{norm}(L) = \frac{\rho(L)}{\rho_{max}(L)}$$

The resulting normalized density profiles were similar for the outer layer of PEGAgNP (52.7 nm) and PEGAuNP (35.7 nm) and are shown in Figure S1 in the *Supplementary Materials*. Finally, the shell was trimmed to match the maximum number of CG beads predicted by Flory theory:

$$n_{CG} = \frac{NA\sigma}{n_{mono}},$$

where  $n_{mono}$  is number of monomer units represented by a single CG bead. For the current model  $n_{mono} = 3$ .

It should be mentioned, that  $n_{CG}$  value for intermediate density brush corresponded to ca. 35% of the reported experimental PEG concentration on NPs. And the full experimental concentration of PEG corresponded to brush densities between the intermediate and brush regimes, suggesting that most likely the high-density regime was reached during the experiment. To evaluate the adsorption affinities for four different grafting density regimes of PEG, labelled “mushroom” ( $n_{CG} = 689(\text{Ag})/459(\text{Au})$ ), “intermediate” ( $n_{CG} = 2034(\text{Ag})/1356(\text{Au})$ ), “custom” ( $n_{CG} = 5236(\text{Ag})/2541(\text{Au})$ ) and “brush” ( $n_{CG} = 20860(\text{Ag})/14143(\text{Au})$ ) were considered (Figure 3).

The *GenerateNanoparticle.py* tool from the UA package<sup>46</sup> was used to assign the coordinates of CG beads to core-shell NPs. The resulting NP coordinate files defining NPs shown in Figure 2

were included in the *Supplementary Materials*. These files (\*.np) supply the coordinates and definition of the material for all the CG beads present in an NP for the *UA* multiscale simulations. To evaluate the adsorption of the proteins three different grafting density regimes of PEG, labelled “mushroom”, “intermediate”, and “brush”, were considered (Table S1 in *Supplementary Materials*).

### **UA calculations of adsorption affinities.**

The experimental values of NP radii and  $\zeta$ -potential were applied for the *UA* modeling of protein adsorption (Table S2, *Supplementary Materials*) for reported proteins<sup>26</sup>. Adsorption affinities for each protein were obtained as an average of the energy of adsorption obtained for three different surfaces of the face-centered cubic structure of the metallic core. In the absence of a specific model for the NP geometry, we take a maximum entropy approach and weight each of the considered surfaces equally such that the average energy for a given protein orientation is given by:

$$E_{ads}(\theta, \phi) = \frac{E_{ads}^{FCC100}(\theta, \phi) + E_{ads}^{FCC110}(\theta, \phi) + E_{ads}^{FCC111}(\theta, \phi)}{3}$$

Since the binding energies are typically similar for each surface, these approximate weights and averaging scheme do not introduce a significant error relative to other errors present in the calculation. The positions of the PEG CG beads remain unchanged during the *UA* multiscale simulations and the protein “scans” the potential energy surface along the z axis, normal to the surface of the core NP. To ensure that various density regions of the PEG shell are sampled by the protein during this scan, 20 rotational configurations were created by random rotation of the

original CG configuration and included in the ensemble. As a result, each PEGAgNP and PEGAuNP with various brush density was represented by 60 CG configurations of nanoparticle (20 rotational configurations  $\times$  3 FCC). Final adsorption energies were averaged for each type of protein (see `2022-11-30_ua_adsorbition_affinities_supporting_materials.csv` file in *Supplementary material*).

The interactions between CG beads of the protein and the NP components were computed separately, with two sets of corresponding short-range surface potentials for the metallic core and polymeric shell on the surface. The parametrized set of short-range surface potentials for the silver FCC 100, 110, 111 surfaces were reported previously<sup>22</sup>. The procedures for obtaining short-range surface potentials for metallic crystalline gold and unstructured PEG are described in the following sections.

#### **Parametrization of short-range nonbonded potentials for zero-valent gold nanomaterial.**

The PMFs for the three Au FCC surfaces reported here differ from the set of Au PMFs reported earlier for use with  $UA^{21}$ . The difference is that the old set included Au(100) FCC configuration only, excluded salt, used different models for some AA SCAs, calculated NP-AA potentials with AMBER03 force field parameters, and employed different settings for the metadynamics, primarily a smaller initial hill height. The (100) surface for FCC gold is predicted to be the least stable out of the low Miller index surfaces (100, 110, 111)<sup>47</sup> and the interactions between Au(100) and AAs were found to be more exothermic than for other surfaces. This led to a consistent overestimation of adsorption affinities calculated for blood plasma proteins<sup>23</sup>. As was mentioned earlier, a more precise description of bio-interfaces for nanosized crystalline materials requires a more realistic interface generated from a combination of surfaces, motivating the inclusion of more Au FCC surfaces and so three Au FCC surfaces were parameterized.

A comprehensive computational protocol for obtaining PMFs for inorganic crystalline materials was reported previously<sup>22,25</sup>. The protocol was based on an adaptive well-tempered metadynamics (AWT-MetaD)<sup>48</sup> scheme included in PLUMED<sup>24</sup> software distribution. All-atom molecular dynamics simulations in this study were performed with Gromacs package. InterfaceFF<sup>49,50</sup> parameters, utilized for Au atoms, were combined with CHARMM36<sup>51</sup> parameters, used for modelling TIP3P water and the “bio” part of the system. Coordinates of the Au slab with three FCC configurations (100, 110, and 111) were obtained from CHARMM-GUI/Nanomaterial Modeler<sup>52</sup>. Thirty-three biomolecular building blocks included in this study are shown in Figure S2 in *Supplementary material*. Solvated “adsorbate-slab” systems were neutralized by 0.15 KCl, corresponding to standard physiological conditions. Obtained simulation boxes (Figure S3 in the *Supplementary materials*) were pre-equilibrated to produce a proper density of aqueous solution around the NP. The temperature was set at 300 K in NPT and NVT ensembles, and the pressure was set at 1 bar in the NPT ensemble. The Nose–Hoover thermostat was invoked for NVT simulations, while Berendsen's weak coupling thermostat and barostat were applied for NPT runs. The system was modelled using periodic boundary conditions (PBC) with the primary cells of 2.4 nm × 2.4 nm × 8.5 nm.

In AWT-MetaD biased simulations producing the desired PMFs, the SSD between NP and the biomolecular building block was sampled in the interval between 0.0 and 2.0 nm. Gaussian hills with an initial height of 2.5 kJ/mol were added along the trajectory every 0.5 ps. The bias factor was set at  $f = 20$ .

The obtained PMFs for gold NPs are shown in Figures S4 and S5 in *Supplementary material* (original files can be also found on Zenodo portal<sup>53</sup>). The PMFs for silver NPs employed here were previously published elsewhere.<sup>22,54</sup>

### **Parametrization of short-range nonbonded potentials for PEG polymeric shell.**

The preliminary tests for applying AWT-MetaD protocol for non-crystalline materials have shown its unsuitability, as smaller adsorbates (e.g., the ALA SCA) were able to penetrate through the polymeric slab, which would not be possible for an actual ALA residue during the adsorption of a protein. Furthermore, due to the extended length of the polymeric chains and their flexibility, a proper sampling of their movement was hard to achieve at recommended trajectory time (400-600 ns). To overcome this problem, a different protocol for generating PMFs for polymeric materials was implemented. The PMF  $w(r)$  describing the pairwise interaction between two atoms (or two CG beads) can be recovered from the radial distribution functions  $g(r)$ <sup>55</sup>:

$$w(r) = -k_B T \ln[g(r)]$$

In this approach, only a short part of the polymer (a trimer) was taken into consideration when modeling the pairwise interaction potentials with the selected biomolecules (Figure S2 in *Supplementary materials*), with this trimer forming a single coarse-grained bead. To recover the pairwise interaction between CG beads of the biopolymer and polymeric nanoparticle, the simulation boxes composed of one AA (or other biomolecular fragment) and 64 PEG trimeric units were solvated and neutralized by 0.15 KCl (Figure S6 in *Supplementary materials*). After pre-equilibration and obtaining a proper density/pressure, production runs of duration 200 ns were performed. The resulted short-range surface potentials for *UnitedAtom Multiscale* model are shown at Figure S7 in *Supplementary materials* (original files can be also found on Zenodo portal<sup>56</sup>). The long-range and electrostatic *UA* interactions were handled as for crystalline materials.

### **Preparation of coordinates for protein structures and adsorption complexes.**

In total, three proteins were studied: BSA, TRF, and ngTRF. Coordinates of BSA and TRF proteins were obtained from the PDB.org portal<sup>57,58</sup>. Glycans were removed from the original TRF PDB files to obtain coordinates for the corresponding structure of ngTRF protein. Protonation states of the proteins were evaluated using PropKa<sup>59</sup> and final coordinates were refined with CHARMM-GUI<sup>52</sup> tools.

*UnitedAtom* calculations were employed utilizing configurational files for core-shell nanoparticles representing different NP structures (see \*.np files in *Supplementary materials*). The results shown in Figures 5 and 6 were obtained by averaging  $E_{ads}(\varphi, \theta)$  values across selected FCC surfaces and 20 rotational CG configurations of nanoparticles ( $i_{conf} = 1 \dots 20$ ):

$$E_{ave}^{i_{conf}}(\varphi, \theta) = \begin{bmatrix} \frac{E_{\varphi=0,\theta=0}^{FCC100} + E_{\varphi=0,\theta=0}^{FCC110} + E_{\varphi=0,\theta=0}^{FCC111}}{3} & \dots & \frac{E_{\varphi=0,\theta=180}^{FCC100} + E_{\varphi=0,\theta=180}^{FCC110} + E_{\varphi=0,\theta=180}^{FCC111}}{3} \\ \vdots & \ddots & \vdots \\ \frac{E_{\varphi=360,\theta=0}^{FCC100} + E_{\varphi=360,\theta=0}^{FCC110} + E_{\varphi=360,\theta=0}^{FCC111}}{3} & \dots & \frac{E_{\varphi=360,\theta=180}^{FCC100} + E_{\varphi=360,\theta=180}^{FCC110} + E_{\varphi=360,\theta=180}^{FCC111}}{3} \end{bmatrix}$$

$$E_{ads}^{ave}(\varphi, \theta) = \begin{bmatrix} \frac{E_{\varphi=0,\theta=0}^{i_{conf}=1} + \dots + E_{\varphi=0,\theta=0}^{i_{conf}=20}}{20} & \dots & \frac{E_{\varphi=0,\theta=180}^{i_{conf}=1} + \dots + E_{\varphi=0,\theta=180}^{i_{conf}=20}}{20} \\ \vdots & \ddots & \vdots \\ \frac{E_{\varphi=360,\theta=0}^{i_{conf}=1} + \dots + E_{\varphi=360,\theta=0}^{i_{conf}=20}}{20} & \dots & \frac{E_{\varphi=360,\theta=180}^{i_{conf}=1} + \dots + E_{\varphi=360,\theta=180}^{i_{conf}=20}}{20} \end{bmatrix}$$

Finally, these NP-averaged adsorption energies were analyzed by an in-house Python script to obtain the positions of local minima and to reconstruct PDB coordinates for adsorption complexes. PDBs coordinates for complexes shown in Figures 7 and 8 are included in *Supplementary materials*. All visualization of structures was done with *NGLView* Python package<sup>60</sup>.

## **Supporting Information.**

The following files are available free of charge.

*Supplementary Materials.*

PDF: contains additional information on the methodology and results of reported multiscale modelling.

TAR file: contains PDBs (structures for protein adsorption complexes discussed in this work), NPs (*UA* configuration files representing nanoparticles), *csv* file with calculated adsorption energies.

## **Corresponding Author**

\*Julia Subbotina, email: [yulia.subbotina@ucd.ie](mailto:yulia.subbotina@ucd.ie)

## **Author Contributions**

The manuscript was written with contributions of all authors. All authors have given approval to the final version of the manuscript.

## **Funding Sources**

This work was supported by Science Foundation of Ireland grant, 16/IA/4506 “Quantitative Modelling of Bionano Interface” and EU Horizon 2020 grant NanoSolveIT, grant agreement 814572.

## **ACKNOWLEDGMENT**

The authors would like to acknowledge the Irish Centre for High-End Computing (ICHEC) and the ResearchIT Sonic cluster, which was funded by UCD IT Services and the Research Office, for the provision of computational facilities and support.

## **ABBREVIATIONS**

NP(s), nanoparticle(s); AuNP, pristine gold nanoparticle; AgNP, pristine silver nanoparticle;

PEGAuNPs, PEGylated gold nanoparticles; PEGAgNPs, PEGylated silver nanoparticles; BSA,

bovine serum albumin; TRF, glycosylated human transferrin; ngTRF, non-glycosylated human transferrin; CG, coarse-grained; MD, molecular dynamics; NM, nanomaterials; PEG, polyethylene glycol; MD, molecular dynamics; *UA Model*, *UnitedAtom Model*; FCC, face-centered cubic; AA, amino acids; SCA, side-chain analogues.

## REFERENCES

- (1) Kłębowski, B.; Depciuch, J.; Parlińska-Wojtan, M.; Baran, J. Applications of Noble Metal-Based Nanoparticles in Medicine. *International Journal of Molecular Sciences*. MDPI AG December 13, 2018. <https://doi.org/10.3390/ijms19124031>.
- (2) Xu, J.; Peng, C.; Yu, M.; Zheng, J. Renal Clearable Noble Metal Nanoparticles: Photoluminescence, Elimination, and Biomedical Applications. *WIREs Nanomedicine and Nanobiotechnology* **2017**, *9* (5), e1453. <https://doi.org/10.1002/wnan.1453>.
- (3) Rai, M.; Ingle, A. P.; Birla, S.; Yadav, A.; Santos, C. A. Dos. Strategic Role of Selected Noble Metal Nanoparticles in Medicine. *Critical Reviews in Microbiology*. Taylor and Francis Ltd September 2, 2016, pp 696–719. <https://doi.org/10.3109/1040841X.2015.1018131>.
- (4) Conde, J.; Doria, G.; Baptista, P. Noble Metal Nanoparticles Applications in Cancer. *J. Drug Deliv.* **2012**, *2012*, 1–12. <https://doi.org/10.1155/2012/751075>.
- (5) Attarilar, S.; Yang, J.; Ebrahimi, M.; Wang, Q.; Liu, J.; Tang, Y.; Yang, J. The Toxicity Phenomenon and the Related Occurrence in Metal and Metal Oxide Nanoparticles: A Brief Review From the Biomedical Perspective. *Frontiers in Bioengineering and Biotechnology*. Frontiers Media S.A. July 17, 2020, p 822. <https://doi.org/10.3389/fbioe.2020.00822>.
- (6) Chandrakala, V.; Aruna, V.; Angajala, G. Review on Metal Nanoparticles as Nanocarriers: Current Challenges and Perspectives in Drug Delivery Systems. *Emergent Materials*. Springer Nature January 4, 2022, pp 1–23. <https://doi.org/10.1007/s42247-021-00335-x>.
- (7) Durán, N.; Silveira, C. P.; Durán, M.; Martinez, D. S. T. Silver Nanoparticle Protein Corona and Toxicity: A Mini-Review. *Journal of Nanobiotechnology*. BioMed Central Ltd.

September 4, 2015, p 55. <https://doi.org/10.1186/s12951-015-0114-4>.

- (8) Perry, J. L.; Reuter, K. G.; Kai, M. P.; Herlihy, K. P.; Jones, S. W.; Luft, J. C.; Napier, M.; Bear, J. E.; Desimone, J. M. PEGylated PRINT Nanoparticles: The Impact of PEG Density on Protein Binding, Macrophage Association, Biodistribution, and Pharmacokinetics. *Nano Lett.* **2012**, *12* (10), 5304–5310. <https://doi.org/10.1021/NL302638G>.
- (9) Mosqueira, V. C. F.; Legrand, P.; Morgat, J. L.; Vert, M.; Mysiakine, E.; Gref, R.; Devissaguet, J. P.; Barratt, G. Biodistribution of Long-Circulating PEG-Grafted Nanocapsules in Mice: Effects of PEG Chain Length and Density. *Pharm. Res.* **2001**, *18* (10), 1411–1419. <https://doi.org/10.1023/A:1012248721523>.
- (10) Chen, G.; Roy, I.; Yang, C.; Prasad, P. N. Nanochemistry and Nanomedicine for Nanoparticle-Based Diagnostics and Therapy. *Chem. Rev.* **2016**, *116* (5), 2826–2885. <https://doi.org/10.1021/ACS.CHEMREV.5B00148>.
- (11) Gheibi Hayat, S. M.; Bianconi, V.; Pirro, M.; Sahebkar, A. Stealth Functionalization of Biomaterials and Nanoparticles by CD47 Mimicry. *International Journal of Pharmaceutics*. Elsevier B.V. October 5, 2019, p 118628. <https://doi.org/10.1016/j.ijpharm.2019.118628>.
- (12) Suk, J. S.; Xu, Q.; Kim, N.; Hanes, J.; Ensign, L. M. PEGylation as a Strategy for Improving Nanoparticle-Based Drug and Gene Delivery. *Advanced Drug Delivery Reviews*. Elsevier B.V. April 1, 2016, pp 28–51. <https://doi.org/10.1016/j.addr.2015.09.012>.
- (13) Gref, R.; Lück, M.; Quellec, P.; Marchand, M.; Dellacherie, E.; Harnisch, S.; Blunk, T.; Müller, R. H. “Stealth” Corona-Core Nanoparticles Surface Modified by Polyethylene Glycol (PEG): Influences of the Corona (PEG Chain Length and Surface Density) and of the Core Composition on Phagocytic Uptake and Plasma Protein Adsorption. *Colloids Surfaces B Biointerfaces* **2000**, *18* (3–4), 301–313. [https://doi.org/10.1016/S0927-7765\(99\)00156-3](https://doi.org/10.1016/S0927-7765(99)00156-3).
- (14) Li, M.; Jiang, S.; Simon, J.; Paßlick, D.; Frey, M. L.; Wagner, M.; Mailander, V.; Crespy, D.; Landfester, K. Brush Conformation of Polyethylene Glycol Determines the Stealth

- Effect of Nanocarriers in the Low Protein Adsorption Regime. *Nano Lett.* **2021**, *21* (4), 1591–1598.  
[https://doi.org/10.1021/ACS.NANOLETT.0C03756/SUPPL\\_FILE/NL0C03756\\_SI\\_001.PDF](https://doi.org/10.1021/ACS.NANOLETT.0C03756/SUPPL_FILE/NL0C03756_SI_001.PDF).
- (15) Cournia, Z.; Allen, B.; Sherman, W. Relative Binding Free Energy Calculations in Drug Discovery: Recent Advances and Practical Considerations. *Journal of Chemical Information and Modeling*. American Chemical Society December 26, 2017, pp 2911–2937. <https://doi.org/10.1021/acs.jcim.7b00564>.
- (16) Duboué-Dijon, E.; Hénin, J. Building Intuition for Binding Free Energy Calculations: Bound State Definition, Restraints, and Symmetry. *J. Chem. Phys.* **2021**, *154* (20), 204101. <https://doi.org/10.1063/5.0046853>.
- (17) Walsh, T. R. Pathways to Structure-Property Relationships of Peptide-Materials Interfaces: Challenges in Predicting Molecular Structures. *Acc. Chem. Res.* **2017**, *50* (7), 1617–1624. [https://doi.org/10.1021/ACS.ACCOUNTS.7B00065/ASSET/IMAGES/LARGE/AR-2017-00065H\\_0004.JPEG](https://doi.org/10.1021/ACS.ACCOUNTS.7B00065/ASSET/IMAGES/LARGE/AR-2017-00065H_0004.JPEG).
- (18) Latour, R. A. Fundamental Principles of the Thermodynamics and Kinetics of Protein Adsorption to Material Surfaces. *Colloids Surfaces B Biointerfaces* **2020**, *191*, 110992. <https://doi.org/10.1016/j.colsurfb.2020.110992>.
- (19) Geada, I. L.; Ramezani-Dakhel, H.; Jamil, T.; Sulpizi, M.; Heinz, H. Insight into Induced Charges at Metal Surfaces and Biointerfaces Using a Polarizable Lennard-Jones Potential. *Nat. Commun.* **2018**, *9* (1), 716. <https://doi.org/10.1038/s41467-018-03137-8>.
- (20) Lopez, H.; Brandt, E. G.; Mirzoev, A.; Zhurkin, D.; Lyubartsev, A.; Lobaskin, V. Multiscale Modelling of Bionano Interface. In *Advances in Experimental Medicine and Biology*; Springer, Cham, 2017; Vol. 947, pp 173–206. [https://doi.org/10.1007/978-3-319-47754-1\\_7](https://doi.org/10.1007/978-3-319-47754-1_7).
- (21) Power, D.; Rouse, I.; Poggio, S.; Brandt, E.; Lopez, H.; Lyubartsev, A.; Lobaskin, V. A Multiscale Model of Protein Adsorption on a Nanoparticle Surface. *Model. Simul. Mater.*

- Sci. Eng.* **2019**, 27 (8), 084003. <https://doi.org/10.1088/1361-651X/ab3b6e>.
- (22) Subbotina, J.; Lobaskin, V. Multiscale Modeling of Bio-Nano Interactions of Zero-Valent Silver Nanoparticles. *J. Phys. Chem. B* **2022**. <https://doi.org/10.1021/ACS.JPCB.1C09525>.
- (23) Alsharif, S. A.; Power, D.; Rouse, I.; Lobaskin, V. In Silico Prediction of Protein Adsorption Energy on Titanium Dioxide and Gold Nanoparticles. *Nanomater.* **2020**, Vol. 10, Page 1967 **2020**, 10 (10), 1967. <https://doi.org/10.3390/nano10101967>.
- (24) Bonomi, M.; Branduardi, D.; Bussi, G.; Camilloni, C.; Provasi, D.; Raiteri, P.; Donadio, D.; Marinelli, F.; Pietrucci, F.; Broglia, R. A.; et al. PLUMED: A Portable Plugin for Free-Energy Calculations with Molecular Dynamics. *Comput. Phys. Commun.* **2009**, 180 (10), 1961–1972. <https://doi.org/10.1016/j.cpc.2009.05.011>.
- (25) Brandt, E. G.; Lyubartsev, A. P. Molecular Dynamics Simulations of Adsorption of Amino Acid Side Chain Analogues and a Titanium Binding Peptide on the TiO<sub>2</sub> (100) Surface. *J. Phys. Chem. C* **2015**, 119 (32), 18126–18139. <https://doi.org/10.1021/acs.jpcc.5b02670>.
- (26) Barbir, R.; Jiménez, R. R.; Martín-Rapún, R.; Strasser, V.; Domazet Jurašin, D.; Dabelić, S.; De La Fuente, J. M.; Vinković Vrček, I. Interaction of Differently Sized, Shaped, and Functionalized Silver and Gold Nanoparticles with Glycosylated versus Nonglycosylated Transferrin. *ACS Appl. Mater. Interfaces* **2021**, 13 (23), 27533–27547. [https://doi.org/10.1021/ACSAMI.1C04063/SUPPL\\_FILE/AM1C04063\\_SI\\_001.PDF](https://doi.org/10.1021/ACSAMI.1C04063/SUPPL_FILE/AM1C04063_SI_001.PDF).
- (27) Hristov, D. R.; Lopez, H.; Ortin, Y.; O’Sullivan, K.; Dawson, K. A.; Brougham, D. F. Impact of Dynamic Sub-Populations within Grafted Chains on the Protein Binding and Colloidal Stability of PEGylated Nanoparticles. *Nanoscale* **2021**, 13 (10), 5344–5355. <https://doi.org/10.1039/D0NR08294E>.
- (28) Malmsten, M.; Emoto, K.; Van Alstine, J. M. Effect of Chain Density on Inhibition of Protein Adsorption by Poly(Ethylene Glycol) Based Coatings. *J. Colloid Interface Sci.* **1998**, 202 (2), 507–517. <https://doi.org/10.1006/jcis.1998.5513>.
- (29) Moghimi, S. M.; Szebeni, J. Stealth Liposomes and Long Circulating Nanoparticles: Critical Issues in Pharmacokinetics, Opsonization and Protein-Binding Properties. *Progress*

- in Lipid Research*. Elsevier Ltd November 1, 2003, pp 463–478. [https://doi.org/10.1016/S0163-7827\(03\)00033-X](https://doi.org/10.1016/S0163-7827(03)00033-X).
- (30) Sun, M.; Deng, J.; Tang, Z.; Wu, J.; Li, D.; Chen, H.; Gao, C. A Correlation Study of Protein Adsorption and Cell Behaviors on Substrates with Different Densities of PEG Chains. *Colloids Surfaces B Biointerfaces* **2014**, *122*, 134–142. <https://doi.org/10.1016/j.colsurfb.2014.06.041>.
- (31) Bhattacharjee, S. M.; Giacometti, A.; Maritan, A. Flory Theory for Polymers. *Journal of Physics Condensed Matter*. IOP Publishing December 18, 2013, p 503101. <https://doi.org/10.1088/0953-8984/25/50/503101>.
- (32) Flory, P. J. *Principles of Polymer Chemistry*; Cornell university press, 1953.
- (33) de Gennes, P. G. Conformations of Polymers Attached to an Interface. *Macromolecules* **1980**, *13* (5), 1069–1075. <https://doi.org/10.1021/ma60077a009>.
- (36) Suk, J. S.; Xu, Q.; Kim, N.; Hanes, J.; Ensign, L. M. PEGylation as a Strategy for Improving Nanoparticle-Based Drug and Gene Delivery. *Advanced Drug Delivery Reviews*. Elsevier B.V. April 1, 2016, pp 28–51. <https://doi.org/10.1016/j.addr.2015.09.012>.
- (37) Faria, M.; Björnmalm, M.; Thurecht, K. J.; Kent, S. J.; Parton, R. G.; Kavallaris, M.; Johnston, A. P. R.; Gooding, J. J.; Corrie, S. R.; Boyd, B. J.; et al. Minimum Information Reporting in Bio–Nano Experimental Literature. *Nat. Nanotechnol.* **2018**, *13* (9), 777–785. <https://doi.org/10.1038/s41565-018-0246-4>.
- (38) Clemente, E.; Martinez-Moro, M.; Trinh, D. N.; Soliman, M. G.; Spencer, D. I. R.; Gardner, R. A.; Kotsias, M.; Sánchez Iglesias, A.; Moya, S.; Monopoli, M. P. Probing the Glycans Accessibility in the Nanoparticle Biomolecular Corona. *J. Colloid Interface Sci.* **2022**, *613*, 563–574. <https://doi.org/10.1016/j.jcis.2021.11.140>.
- (39) Subbotina, J.; Lobaskin, V. Multiscale Modeling of Bio-Nano Interactions of Zero-Valent Silver Nanoparticles. **2021**. <https://doi.org/10.26434/CHEMRXIV-2021-5RSR2>.
- (40) Trinh, D. N.; Gardner, R. A.; Franciosi, A. N.; McCarthy, C.; Keane, M. P.; Soliman, M.

- G.; O'Donnell, J. S.; Meleady, P.; Spencer, D. I. R.; Monopoli, M. P. Nanoparticle Biomolecular Corona-Based Enrichment of Plasma Glycoproteins for N-Glycan Profiling and Application in Biomarker Discovery. *ACS Nano* **2022**, *16* (4), 5463–5475. <https://doi.org/10.1021/acsnano.1c09564>.
- (41) Wan, S.; Kelly, P. M.; Mahon, E.; Stöckmann, H.; Rudd, P. M.; Caruso, F.; Dawson, K. A.; Yan, Y.; Monopoli, M. P. The “Sweet” Side of the Protein Corona: Effects of Glycosylation on Nanoparticle-Cell Interactions. *ACS Nano* **2015**, *9* (2), 2157–2166. [https://doi.org/10.1021/NN506060Q/SUPPL\\_FILE/NN506060Q\\_SI\\_001.PDF](https://doi.org/10.1021/NN506060Q/SUPPL_FILE/NN506060Q_SI_001.PDF).
- (42) Ardawi, M. S. M.; Nasrat, H. N.; Mira, S. A.; Fatani, H. H. Comparison of Glycosylated Fibrinogen, Albumin, and Haemoglobin as Indices of Blood Glucose Control in Diabetic Patients. *Diabet. Med.* **1990**, *7* (9), 819–824. <https://doi.org/10.1111/j.1464-5491.1990.tb01499.x>.
- (43) O'Callahan, B.; Qafoku, O.; Balema, V.; Negrete, O. A.; Passian, A.; Engelhard, M. H.; Waters, K. M. Atomic Force Microscopy and Infrared Nanospectroscopy of COVID-19 Spike Protein for the Quantification of Adhesion to Common Surfaces. *Langmuir* **2021**, *37* (41), 12089–12097. <https://doi.org/10.1021/acs.langmuir.1c01910>.
- (44) Danquah, M. K.; Jeevanandam, J. Cytotoxicity of Nanoparticles toward Diabetic Cell Models. In *Emerging Nanomedicines for Diabetes Mellitus Theranostics*; Elsevier, 2022; pp 173–198. <https://doi.org/10.1016/b978-0-323-85396-5.00005-1>.
- (45) Lopez, H.; Lobaskin, V. Coarse-Grained Model of Adsorption of Blood Plasma Proteins onto Nanoparticles. *J. Chem. Phys.* **2015**, *143* (24), 243138. <https://doi.org/10.1063/1.4936908>.
- (46) Bitbucket <https://bitbucket.org/softmattergroup/> (accessed Dec 11, 2020).
- (47) mp-81: Au (cubic, Fm-3m, 225) <https://materialsproject.org/materials/mp-81/> (accessed Aug 9, 2022).
- (48) Barducci, A.; Bussi, G.; Parrinello, M. Well-Tempered Metadynamics: A Smoothly Converging and Tunable Free-Energy Method. *Phys. Rev. Lett.* **2008**, *100* (2), 020603.

<https://doi.org/10.1103/PhysRevLett.100.020603>.

- (49) Toman, R. *Coxiella Burnetii : Recent Advances and New Perspectives in Research of the Q Fever Bacterium*; Springer, 2012.
- (50) Heinz, H.; Ramezani-Dakhel, H. Simulations of Inorganic-Bioorganic Interfaces to Discover New Materials: Insights, Comparisons to Experiment, Challenges, and Opportunities. *Chem. Soc. Rev.* **2016**, *45* (2), 412–448. <https://doi.org/10.1039/c5cs00890e>.
- (51) Huang, J.; Rauscher, S.; Nawrocki, G.; Ran, T.; Feig, M.; De Groot, B. L.; Grubmüller, H.; MacKerell, A. D. CHARMM36m: An Improved Force Field for Folded and Intrinsically Disordered Proteins. *Nat. Methods* **2016**, *14* (1), 71–73. <https://doi.org/10.1038/nmeth.4067>.
- (52) Jo, S.; Kim, T.; Iyer, V. G.; Im, W. CHARMM-GUI: A Web-Based Graphical User Interface for CHARMM. *J. Comput. Chem.* **2008**, *29* (11), 1859–1865. <https://doi.org/10.1002/jcc.20945>.
- (53) Subbotina, J. *United Atom Parameters for United Atom Multiscale Modelling Of Bio-Nano Interactions Of Zero-Valent Gold Nanoparticles*; 2022. <https://doi.org/https://doi.org/10.5281/zenodo.6066434>.
- (54) Subbotina, Y. *United Atom Parameters for United Atom Multiscale Modelling Of Bio-Nano Interactions Of Zero-Valent Silver Nanoparticles*. **2022**. <https://doi.org/10.5281/ZENODO.5846080>.
- (55) Sippl, M. J.; Ortner, M.; Jaritz, M.; Lackner, P.; Flöckner, H. Helmholtz Free Energies of Atom Pair Interactions in Proteins. *Fold. Des.* **1996**, *1* (4), 289–298. [https://doi.org/10.1016/S1359-0278\(96\)00042-9](https://doi.org/10.1016/S1359-0278(96)00042-9).
- (56) Subbotina, J. *United Atom Parameters for United Atom Multiscale Modelling Of Bio-Nano Interactions Of PEG Coated Nanoparticles*. **2022**. <https://doi.org/10.5281/ZENODO.6066503>.
- (57) Majorek, K. A.; Porebski, P. J.; Dayal, A.; Zimmerman, M. D.; Jablonska, K.; Stewart, A.

- J.; Chruszcz, M.; Minor, W. Structural and Immunologic Characterization of Bovine, Horse, and Rabbit Serum Albumins. *Mol. Immunol.* **2012**, *52* (3–4), 174–182. <https://doi.org/10.1016/j.molimm.2012.05.011>.
- (58) Wally, J.; Halbrooks, P. J.; Vornrhein, C.; Rould, M. A.; Everse, S. J.; Mason, A. B.; Buchanan, S. K. The Crystal Structure of Iron-Free Human Serum Transferrin Provides Insight into Inter-Lobe Communication and Receptor Binding. *J. Biol. Chem.* **2006**, *281* (34), 24934–24944. <https://doi.org/10.1074/jbc.M604592200>.
- (59) Jurrus, E.; Engel, D.; Star, K.; Monson, K.; Brandi, J.; Felberg, L. E.; Brookes, D. H.; Wilson, L.; Chen, J.; Liles, K.; et al. Improvements to the APBS Biomolecular Solvation Software Suite. *Protein Sci.* **2018**, *27* (1), 112–128. <https://doi.org/10.1002/pro.3280>.
- (60) Nguyen, H.; Case, D. A.; Rose, A. S. NGLview–Interactive Molecular Graphics for Jupyter Notebooks. *Bioinformatics* **2018**, *34* (7), 1241–1242. <https://doi.org/10.1093/BIOINFORMATICS/BTX789>.